



LAWRENCE  
LIVERMORE  
NATIONAL  
LABORATORY

# An $O(N \log N)$ multi-layer boundary element method for direct computation of sound propagation in shallow water environments

C. Li, B. K. Campbell, Y. Liu, D. K.P. Yue

November 7, 2018

Proceedings of the royal society of London A: mathematical physical and engineering sciences

## **Disclaimer**

---

This document was prepared as an account of work sponsored by an agency of the United States government. Neither the United States government nor Lawrence Livermore National Security, LLC, nor any of their employees makes any warranty, expressed or implied, or assumes any legal liability or responsibility for the accuracy, completeness, or usefulness of any information, apparatus, product, or process disclosed, or represents that its use would not infringe privately owned rights. Reference herein to any specific commercial product, process, or service by trade name, trademark, manufacturer, or otherwise does not necessarily constitute or imply its endorsement, recommendation, or favoring by the United States government or Lawrence Livermore National Security, LLC. The views and opinions of authors expressed herein do not necessarily state or reflect those of the United States government or Lawrence Livermore National Security, LLC, and shall not be used for advertising or product endorsement purposes.



**Subject Areas:**

ocean engineering, acoustics,  
computer modeling and simulation

**Keywords:**

Shallow Water Acoustics,  
Pre-corrected Fast Fourier Transform  
Method, Boundary Element Method

**Author for correspondence:**

Dick K.P. Yue

e-mail: [yue@mit.edu](mailto:yue@mit.edu)

# An $O(N \log N)$ multi-layer boundary element method for direct computation of sound propagation in shallow water environments

Chengxi Li<sup>1</sup>, Bryce Campbell<sup>1,2</sup>, Yuming Liu<sup>1</sup> and Dick K.P. Yue<sup>1</sup>

<sup>1</sup>Department of Mechanical Engineering,  
Massachusetts Institute of Technology, Cambridge,  
MA, 02139, USA

<sup>2</sup>Also at: Center for Applied Scientific Computing,  
Lawrence Livermore National Laboratory, Livermore,  
CA, 94551, USA

Direct three-dimensional (3D) numerical simulations of acoustic fields in range-dependent shallow water environments remains a challenge due to environmental complexities and large computational cost. We develop an efficient 3D boundary element method (BEM) for shallow water acoustic propagation which utilizes a Pre-corrected Fast Fourier Transform (PFFT) approach to reduce the computational effort from  $O(N^{2\sim 3})$  to  $O(N \log N)$  where  $N$  is the total number of boundary unknowns. To account for inhomogeneous media, the method allows for arbitrary number of coupled multi-layer BEM sub-domains. With  $O(N \log N)$  efficiency and the use of massively parallel high-performance computing platforms, we are able to conduct multi-layer 3D direct simulations of low-mid frequency acoustics over kilometer ranges. We perform extensive validations of the method and provide two shallow water waveguide examples benchmarked against theoretical solutions. To illustrate the efficacy and usefulness of the PFFT-BEM method, we perform 3D large-scale direct simulations to assess the performance of two established canonical models: axisymmetric coupled mode model for 3D seamount; and Kirchhoff approximation and perturbation theory for 3D rough surface scattering.

## 1. Introduction

Prediction of a 3D underwater sound field in range-dependent shallow water environments, involving complex domain geometry and water properties, is a challenging and active research area. Over the years, a number of propagation models have been proposed, generally based on some limiting assumptions or approximations. Notable among these are the ray tracing model, the coupled mode model and the parabolic equation (PE) model. Ray tracing models (e.g. Bucker [1]; Porter [2]) are based on an underlying high-frequency assumption and are generally not valid for low-mid frequencies. Furthermore, they are usually applied only to 2D problems because of the substantial computational cost of full 3D ray tracing calculations (Jensen *et al.* [3]).

For specialized geometries, the coupled mode method [3] can be powerful, for example, when applied to 3D conical seamount with vertical axisymmetry [4]. When environmental properties are invariant along a spatial coordinate, the two-dimensional (2D) coupled mode method can be combined with a wavenumber integration method to obtain 3D acoustic fields [5,6]. For slowly-varying spatial environments in two directions, a simplified coupled mode model, the adiabatic-mode model, has also proven useful (e.g. Badiéy *et al.* [7]; Ballard [8]; Lynch *et al.* [9]). For general 3D geometries, a fully coupled mode propagation model is still impractical due to large computing power and memory requirements [3].

A large class of propagation models are based on the one-way parabolic equation (PE) approximation [10]. For 3D applications where backscattering is not significant, a number of PE models have been developed (e.g. Lin *et al.* [11,12]; Sturm [13]). Models that include two-way scattering have been developed in general 2D [14,15], and for 3D formulated in cylindrical coordinates [16], valid within a limited domain. Hybrid normal mode/PE method (e.g. Ballard *et al.* [17]) has been developed to account for outgoing mode-coupling and horizontal refraction effects but is valid only when backscattering and modal coupling in the azimuthal direction are weak. Xu *et al.* [18] provides a survey of PE approximations highlighting the efficacies, and limitations especially for complex 3D problems.

With the continuing increase in computational power, there has been a rise in direct acoustic simulations wherein the wave equation is solved directly without additional assumptions. These direct solutions typically involve volume discretization or boundary surface paneling (see Jensen *et al.* [3] for review). The former includes finite difference method (FDM), finite element method (FEM), finite volume method (FVM), and spectral element method (SEM). Because of the large number of volume discretized unknowns, these methods are generally more successful and mainly practical for 2D applications (e.g. Bottero *et al.* [19]; Santiago & Wrobel [20]; Vendhan *et al.* [21]; [19,24]). A longitudinally-invariant FEM has recently been proposed [22], which can provide a 3D sound field with the constraint that the geometry of environments is constant along one of the three spatial coordinates. A 3D SEM has also been recently developed for low frequency [23]. Largely due to prohibitive computational costs, 3D simulations of realistic ocean acoustics using volume-discretization methods remains a significant challenge.

The number of unknowns is reduced in boundary element methods (BEM) where only the boundary of the domain is discretized. In the BEM, the Helmholtz boundary-value problem for homogeneous medium is formulated as a boundary integral equation (BIE) (e.g. Burton and Miller [25]), for which the unknown pressure or normal pressure gradient on the boundary of the medium are solved. After discretizing the boundary into piecewise elements and approximating the variables over these elements, we obtain a system of linear algebraic equations of the form:  $\mathbf{Ax} = \mathbf{b}$ , where  $\mathbf{A}$  is a dense  $N \times N$  influence coefficient matrix,  $\mathbf{x}$  is the vector of  $N$  unknown pressures or/and normal pressure gradient on the boundary, and  $\mathbf{b}$  the vector of known quantities. A number of 2D or 2.5D (longitudinally-invariant) BEM shallow water waveguide solutions exist (e.g. Godinho *et al.* [26]; Pereira [27]); and BEM have been applied to 3D acoustical radiation and scattering problem from rigid bodies (e.g. Keuchel *et al.* [28]; Yan & Gao [29]). While BEM can handle complex boundaries and domain interfaces, its major drawback is the computation cost associated with the solution system involving dense influence matrices  $\mathbf{A}$ .

Existing approaches using (direct or) iterative solvers [30] require  $O(N^2)$  operations and memory to construct and store the influence matrix  $\mathbf{A}$ , and ( $O(N^3)$  or  $O(N^2)$ ) operations for the solution  $\mathbf{x}$ . For realistic 3D direct acoustics simulations over kilometer ranges even for low-mid frequencies,  $N$  can be  $\gtrsim O(10^{7\sim 10})$  (see examples in §§3, 4), and direct 3D simulations using BEM is still not practical.

In this work, we implement a direct solution of the 3D acoustic problem for range-dependent shallow-water environments with complex boundaries using BEM. To account for inhomogeneity of the medium properties, we develop a multi-domain (multi-layer) approach [27] where homogeneous properties are assumed within each sub-domain. The overall solution is obtained by imposing continuity of pressure and normal pressure gradient at the interfaces of the sub-domains. The major development here is the adaptation of a Pre-corrected Fast Fourier Transform (PFFT) approach to reduce the overall computational effort from  $O(N^{2\sim 3})$  to  $O(N \log N)$ . PFFT has been applied to accelerate the BEM in solving the boundary-value problems in the fields of electrostatic analysis [31,54], elastodynamics [53,55], solid mechanics [56], hydrodynamics [32] and rigid-body acoustics scattering [29]. A special property of the method is that the PFFT accelerated BEM (PFFT-BEM) is particularly suitable for massive parallelization [32], which we develop and implement on modern high-performance computing (HPC) platforms.

To establish the accuracy and convergence of the PFFT-BEM, we perform extensive validation of the PFFT-BEM for 3D large-scale benchmark problems including (i) sound propagation in a two-layer shallow-water ocean environment (i.e. the classical Pekeris waveguide) [3]; (ii) sound propagation in realistic ocean environment with inhomogeneous sound profile; (iii) sound transmission field in the Acoustical Society of America (ASA) benchmark wedge [33]; (iv) sound scattering by a 3D underwater seamount [4]; (v) sound propagation in shallow water with a Gaussian canyon on the bottom; (vi) sound scattering by traveling internal waves; and (vii) sound propagation in the Mouth of the Columbia River (MCR), USA. The PFFT-BEM predictions match the existing analytic or benchmark numerical solutions or available field measurements very well for all these cases. For illustration, we present the validation results in this paper for (i), (iii) and (iv) while the comparisons for (ii), (v), (vi) and (vii) can be found in [57].

Large-scale direct solutions using PFFT-BEM are very useful, among other applications, for assessing the range of validity and performance of established approximate or specialized models. To illustrate this, we benchmark direct PFFT-BEM solutions for two problems: (a) axisymmetric coupled mode model for sound scattering by a 3D underwater seamount; and (b) Kirchhoff approximation and perturbation theory for 3D rough surface scattering. For problem (a), we first validate the PFFT-BEM solution to the coupled mode method for the (axisymmetric) conical seamount for which the latter is valid, and then we compare the different solutions to characterize and quantify the effects of varying seamount geometries (seamount height and cross section shape) and sound source frequencies. For problem (b), we assess the accuracy of established approximation models through quantitative comparisons with direct PFFT-BEM simulations. We identify and quantify regions of validity of the former in terms of 3D scattering effects, surface roughness and correlation length, and incidence angle of the sound source.

## 2. PFFT accelerated BEM

### (a) Coupled multi-layer boundary element method

We start with the 3D (spatial) Helmholtz wave equation for a harmonic sound wave:

$$\rho(\vec{x}, t) \nabla \cdot \left( \frac{1}{\rho(\vec{x}, t)} \nabla p(\vec{x}) \right) + k^2 p(\vec{x}) = 0 \quad \vec{x} \in V \quad (2.1)$$

where  $\vec{x}=(x, y, z)$ ,  $t$  is time,  $p(\vec{x})$  the sound pressure,  $\nabla$  the gradient operator,  $\rho(\vec{x}, t)$  the medium density,  $V$  the entire domain volume, and  $k$  the medium wavenumber. The problem is subject to

the pressure release boundary condition at the water free surface  $S_F$ :

$$p(\vec{x}) = 0 \quad \vec{x} \in S_F. \quad (2.2)$$

Sommerfeld radiation condition is satisfied at the far-field boundary  $S_\infty$ :

$$\frac{\partial p(\vec{x})}{\partial n} - ikp(\vec{x}) = 0 \quad \vec{x} \rightarrow \infty \quad (2.3)$$

where  $n$  is the boundary normal. In addition to penetrable bottom or body boundary conditions, Neumann boundary condition can also be imposed on rigid bottom/body boundaries  $S_B$ :

$$\frac{\partial p(\vec{x})}{\partial n} = 0 \quad \vec{x} \in S_B. \quad (2.4)$$

Inhomogeneous medium properties are accounted for by decomposing  $V$  into sub-domains  $V_i$  within which  $\rho = \rho_i(t)$  and  $k = k_i(t)$  are assumed to be constant at any time. For  $p = p^i$  in  $V_i$ , we impose matching conditions across sub-domain boundaries  $S_{ij}$  between sub-domains  $V_i, V_j$  for continuity of pressure  $p$  and particle velocity  $\vec{u}$ :

$$p^i = p^j; \quad \frac{1}{\rho_i} p_n^i = \frac{1}{\rho_j} p_n^j, \quad \vec{x} \in S_{ij}. \quad (2.5)$$

This completes the boundary-value problem.

From Green's second theorem, the boundary integral equation (BIE) for the pressure  $p^i(\vec{x})$  in each layer ( $\vec{x} \in V_i$ ) is

$$4\pi p^i(\vec{x}) - \iint_{S_i} p_n^i(\vec{\zeta}) G(\vec{x}; \vec{\zeta}) dS_i(\vec{\zeta}) + \iint_{S_i} p^i(\vec{\zeta}) G_n(\vec{x}; \vec{\zeta}) dS_i(\vec{\zeta}) = 0 \quad (2.6)$$

where  $S_i$  is the boundary of sub-domain  $V_i$ . Here  $G(\vec{x}; \vec{\zeta}) = |\vec{x} - \vec{\zeta}|^{-1} e^{ik|\vec{x} - \vec{\zeta}|}$  is the Green function which satisfies the Helmholtz equation, and  $\vec{\zeta}$  is any point on  $S_i$ .

For simplicity, for the present shallow-water applications, we consider multi-layer [27] sub-domains  $V_i, i=1, 2, \dots, I$ , where  $S_1$  is the free surface  $S_F$ , and  $S_I$  is the (penetrable unbounded) bottom ( $S_B$  is not used). Taking the limit  $\vec{x} \rightarrow S_i$  in Eq.(2.6) and using boundary conditions Eq.(2.2), Eq.(2.3) and Eq.(2.5), the BIE for each layer can be coupled into a single integral equation in the form:

$$\begin{cases} - \iint_{\hat{S}_1} \hat{p}_n^1(\vec{\zeta}) G(\vec{x}; \vec{\zeta}) d\hat{S}_1(\vec{\zeta}) + \beta_1 \iint_{\hat{S}_1} \hat{p}_n^2(\vec{\zeta}) G(\vec{x}; \vec{\zeta}) d\hat{S}_1(\vec{\zeta}) + \iint_{\hat{S}_1} \hat{p}^2(\vec{\zeta}) G_n(\vec{x}; \vec{\zeta}) d\hat{S}_1(\vec{\zeta}) \\ + \alpha \hat{p}^2(\vec{x}) = 4\pi f_s e^{ik|\vec{x} - \vec{x}_s|} |\vec{x} - \vec{x}_s|^{-1}, & \vec{x} \in S_1 \\ - \iint_{\hat{S}_i} \hat{p}_n^i(\vec{\zeta}) G(\vec{x}; \vec{\zeta}) d\hat{S}_i(\vec{\zeta}) + \iint_{\hat{S}_i} \hat{p}^i(\vec{\zeta}) G_n(\vec{x}; \vec{\zeta}) d\hat{S}_i(\vec{\zeta}) + \beta_i \iint_{\hat{S}_i} \hat{p}_n^{i+1}(\vec{\zeta}) G(\vec{x}; \vec{\zeta}) d\hat{S}_i(\vec{\zeta}) \\ + \iint_{\hat{S}_i} \hat{p}^{i+1}(\vec{\zeta}) G_n(\vec{x}; \vec{\zeta}) d\hat{S}_i(\vec{\zeta}) + \alpha p^i(\vec{x}) = 0, & \vec{x} \in S_2, \dots, I-1 \\ \alpha p^I(\vec{x}) - \iint_{\hat{S}_I} \hat{p}_n^I(\vec{\zeta}) G(\vec{x}; \vec{\zeta}) d\hat{S}_I(\vec{\zeta}) + \iint_{\hat{S}_I} \hat{p}^I(\vec{\zeta}) G_n(\vec{x}; \vec{\zeta}) d\hat{S}_I(\vec{\zeta}) = 0, & \vec{x} \in S_I \end{cases} \quad (2.7)$$

where  $\alpha$  is the solid angle at  $\vec{x}$  on the boundary,  $f_s$  is the strength of a point source located at  $\vec{x}_s$  in layer 1,  $\beta_i = \rho_i / \rho_{i+1}$ ,  $\hat{S}_i, \check{S}_i$  refer respectively to the upper and lower boundary of layer  $V_i$ , and principle value integrals are indicated. It should be noted that the Green's function satisfies the Sommerfeld condition Eq.(2.3) and  $S_\infty$  does not appear in Eq.(2.7) [27,34].

At this point, we discretize the boundaries in Eq.(2.7) into boundary elements with piecewise continuous values of  $p$  and  $p_n$  within each element. The discretization choice can be quite general. For simplicity, we use Constant Panel Method (CPM) using piecewise linear quadrilateral elements with constant values of  $p$  and  $p_n$  in each element, and element centroid collocation. After some assemblage, Eq.(2.7) can be cast as a system of linear algebraic equations of the form:

$$\begin{cases} 2\pi \hat{p}^2(\vec{x}) - \sum_{j=1}^{N^1} (\hat{F}_s^1)_j + \sum_{j=1}^{N^2} [\beta_1 (\hat{F}_s^2)_j + (\hat{F}_d^2)_j] = 4\pi f_s e^{ik|\vec{x} - \vec{x}_s|} |\vec{x} - \vec{x}_s|^{-1}, & \vec{x} \in S_1 \\ 2\pi p^i(\vec{x}) - \sum_{j=1}^{N^i} [(\hat{F}_s^i)_j - (\hat{F}_d^i)_j] + \sum_{j=1}^{N^{i+1}} [\beta_i (\hat{F}_s^{i+1})_j + (\hat{F}_d^{i+1})_j] = 0, & \vec{x} \in S_2, \dots, I-1 \\ 2\pi p^I(\vec{x}) - \sum_{j=1}^{N^I} [(\hat{F}_s^I)_j + (\hat{F}_d^I)_j] = 0, & \vec{x} \in S_I \end{cases} \quad (2.8)$$

$$(\hat{F}_s^i)_j = (\hat{p}_n^i)_j \iint_{E_j} G(\vec{x}; \vec{\zeta}) d\hat{S}_i(\vec{\zeta}); \quad (\hat{F}_d^i)_j = (\hat{p}^i)_j \iint_{E_j} G_{n(\vec{\zeta})}(\vec{x}; \vec{\zeta}) d\hat{S}_i(\vec{\zeta}); \quad (2.9)$$

where  $E_j$  is the  $j^{th}$  element and  $N^i$  the total number of elements in  $i^{th}$  layer. Here,  $\alpha=2\pi$  at the collocation point within CPM. Finally, we express Eq.(2.8) in symbolic form:

$$[A] \{x\} = \{b\} \quad (2.10)$$

where  $[A]$ ,  $N \times N$  is dense and nonsymmetric, and  $N = \sum_{i=1}^I N^i$ . The assemblage of  $[A]$  requires  $O(N^2)$  effort, while  $[A]$  itself requires  $O(N^2)$  memory. A direct solution of Eq.(2.10) would in general requires  $O(N^3)$  effort, while a good iterative solver would use  $O(N^2)$  operations. With  $O(N^2)$  memory and CPU requirements, realistic applications would be limited to  $N \sim O(10^{4 \sim 5})$  on modern HPC platforms, corresponding to say a 100Hz frequency in a 3D domain of (horizontal) dimension  $\sim 100\text{m}$ .

A key development of this work is the solution of Eq.(2.10) using  $O(N)$  memory (without explicitly forming the influence matrix  $[A]$ ) and  $O(N \log N)$  operations. This is accomplished using a Pre-corrected Fast Fourier Transform (PFFT) algorithm.

### (b) Evaluation of matrix-vector product using PFFT acceleration

To illustrate the underlying approach in PFFT-BEM, we first consider forming the pressure  $p(\vec{x})$  at field point  $\vec{x}$  due to a source ( $G(\vec{x}; \vec{\zeta})$ ) distribution on  $N$  boundary elements on  $S$ :

$$p(\vec{x}) = \sum_{j=1}^N \iint_{E_j} \sigma(\vec{\zeta}) G(\vec{x}; \vec{\zeta}) dS(\vec{\zeta}) = \sum_{j=1}^N I_{sj}(\vec{x}) \quad (2.11)$$

where  $\sigma(\vec{\zeta})$  is the source strength distribution, and  $I_{sj}$  is the contribution to  $p(\vec{x})$  due to source distribution on element  $E_j$ . In BEM,  $p(\vec{x})$  must be evaluated at  $N$  collocation points  $\vec{x}_j$ ,  $j=1, 2, \dots, N$  on the BEM boundary  $S$ . This evaluation can be accomplished in  $O(N \log N)$  using PFFT in five steps:

(1) *Grid definition*: We identify a 3D block that contains the  $N$  boundary elements. By subdividing this 3D block into a grid of small cubes, each differential cube will contain a number of boundary elements. Each of these small cubes is referred to as a cell. By temporarily computing the pressures on the cell grid points, we can account for the distant interactions by using only a few weighted local pressure cell values. Furthermore, by evaluating these pressures on a uniform grid, the pressure evaluation has the form of a convolution (will be derived in the projection step) which allows for it to be evaluated with FFTs. Interpolation and correction steps are then taken at the end of the algorithm to adjust the solution from the cell values back to the boundary element mesh. Our algorithm constructs this surrounding grid using  $N_x \times N_y \times N_z$  uniform grid in the  $x$ -,  $y$ -,  $z$ -directions (with  $N_g \equiv N_x \times N_y \times N_z$ ). Note that the grid size  $h$  does not necessarily need to be identical in the three directions. Without loss of generality,  $h$  is considered to be constant in this paper.

(2) *Projection*: In this step, the source distribution in Eq.(2.11) is projected to point sources at the  $v^3$  ( $v \geq 2$ ) vertices of the cell which contains the boundary element  $E_j$ . An accurate projection must satisfy the requirement that the  $p(\vec{x})$  obtained from the net influence of the point source at cell vertices must be identical to that of the original source distribution on the elements.

To do that, we first represent the Green function  $G(\vec{x}; \vec{\zeta})$  (i.e.  $p(\vec{x})$  results from a unit point source at  $\vec{\zeta}$ ) by the net influence of point sources at the vertices of the cell which covers point source  $G(\vec{x}; \vec{\zeta})$ :

$$G(\vec{x}; \vec{\zeta}) = \sum_{m=1}^{v^3} H_m(\vec{\zeta}) G(\vec{x}; \vec{\zeta}_m) \quad (2.12)$$

where  $\vec{\zeta}_m$  is the coordinate of the  $m^{th}$  vertex of the cell which covers the element  $E_j$  and  $H_m$  is the spatial interpolation function for the  $m^{th}$  vertex of the cell. The details of the method for

constructing  $H_m$  can be found in [32] or [57]. Using (2.12), we have

$$I_{sj}(\vec{x}) = \iint_{E_j} \sigma(\vec{\zeta}) G(\vec{x}; \vec{\zeta}) dS(\vec{\zeta}) = \sum_{m=1}^{v^3} q_{jm} G(\vec{x}; \vec{\zeta}_m) \quad (2.13)$$

where

$$q_{jm} = \sigma(\vec{\zeta}) \iint_{E_j} H_m(\vec{\zeta}) dS(\vec{\zeta}) \quad (2.14)$$

Eq.(2.14) is used to determine the strength of the projected point source,  $q_{jm}$ , at  $m^{th}$  vertex of the cell associated with the  $j^{th}$  element. After taking the summation of all the projections of the boundary elements associated with the uniform 3D FFT grid  $n$ , the total strength of the point source at  $n^{th}$  grid  $q_n$  is given by

$$q_n = \sum_{j=1}^{N_n} q_{jn} \quad (2.15)$$

with  $n = 0, 1, \dots, N_g - 1$ ,  $N_n$  represents the total number of boundary elements associated with the uniform 3D FFT grid  $n$ .

(3) Convolution: We evaluate the pressure at the 3D grid points due to point sources at these grids as

$$p_l = \sum_{n=0}^{N_g-1} q_n G_{l-n} \quad l = 0, 1, \dots, N_g - 1 \quad (2.16)$$

where  $G_{l-n} = \frac{1}{|x_l - x_n|} e^{ik|x_l - x_n|}$ . The Fast Fourier Transform (FFT) is used to evaluate Eq.(2.16) efficiently as it is in a convolution form. Before directly applying FFT, the forms of the  $G$  and  $q$  terms need to be modified since the total number of  $G$  terms differs from that of  $q$  and due to  $G_0$  being singular. To do this, we first define a function  $P$  as

$$P_l = \sum_{n=-N_g+1}^{N_g-1} q'_n G'_{l-n}, \quad l = -N_g + 1, \dots, 0, 1, \dots, N_g - 1 \quad (2.17)$$

where  $q'$  and  $G'$  are periodic with the same period  $(2N_g - 1)$  and are defined as

$$G'_{l-n} = \begin{cases} 0, & l = n, \\ G_{l-n}, & -N_g + 1 \leq l - n \leq N_g - 1 \text{ and } l \neq n \end{cases} \quad (2.18)$$

and

$$q'_n = \begin{cases} 0, & -N_g + 1 \leq n \leq 0, \\ q_n, & 0 \leq n \leq N_g - 1. \end{cases} \quad (2.19)$$

and Eq.(2.17) is now in the convolution form of two discrete periodic functions. Therefore, FFTs can be directly applied to evaluate  $P_l$  for a given  $q'$  and  $G'$  with a computational cost of  $O(N_g \log N_g)$ . With the self influence excluded from  $p$  in Eq.(2.16), we have  $p_l = P_l$ ,  $l = 0, 1, \dots, N_g - 1$  (the self influence of point source will be added to solution in the step of near field correction).

(4) Interpolation: In this step, we evaluate  $p(\vec{x})$  on the boundary elements using the interpolation function  $H_m$  based on the grid values  $p_l$  obtained in the convolution step. The form of  $p(\vec{x})$  can now be expressed as

$$p(\vec{x}) = \sum_{m=1}^{v^3} H_m(\vec{x}) p(\vec{\zeta}_m), \quad (2.20)$$

where  $m$  is the  $m^{th}$  vertex of the cell surrounds the element located at  $\vec{x}$ .

(5) Near field correction: Finally we correct the near field part of  $p(\vec{x})$  evaluated by FFT based on Eq.(2.13). This is due to the fact that when  $|\vec{x} - \vec{\zeta}|/h \leq O(1)$ , the accuracy of representation of  $G(\vec{x}; \vec{\zeta})$  by  $G(\vec{x}; \vec{\zeta}_m)$ ,  $m=1, \dots, v^3$  deteriorates. In this step, the near field contribution evaluated in



the convolution step and the exact near field contribution obtained using direct computation is subtracted and added to the solution, respectively. The correction  $\Delta p(\vec{x})$  is represented as

$$\Delta p(\vec{x}) = p_N(\vec{x}) - p_{FN}(\vec{x}) \quad (2.21)$$

where  $p_{FN}(\vec{x})$  is the near-field part of the influence obtained from Eq.(2.20) based on the results in convolution step and  $p_N(\vec{x})$  is the exact influence of the near-field elements determined by directly evaluating the boundary element integrals in Eq.(2.11). Then, the final result of  $p(\vec{x})$ :

$$p(\vec{x}) = p_F(\vec{x}) + \Delta p(\vec{x}) \quad (2.22)$$

where  $p_F(\vec{x})$  is the total influence results evaluated from the convolution step. In practical implementation, the near/far field is defined for  $|\vec{x} - \vec{\zeta}| \leq / > d$  with the distance  $d$  being determined by numerical convergence tests (see figure 1(a)).

The evaluation of  $p_n$  due to a dipole distribution using PFFT algorithm can be accomplished in a similar manner. The normal gradient of the pressure  $p_n(\vec{x})$  at  $\vec{x}$  due to the influence of the dipole distribution with strength  $\gamma(\vec{\zeta})$  on a surface  $S$  is given by:

$$p_n(\vec{x}) = \iint_S \gamma(\vec{\zeta}) G_{n(\vec{\zeta})}(\vec{x}; \vec{\zeta}) dS(\vec{\zeta}) = I_\zeta(\vec{x}) + I_\eta(\vec{x}) + I_\xi(\vec{x}) \quad (2.23)$$

$$I_\chi(\vec{x}) = \iint_S n_\chi(\vec{\zeta}) \gamma(\vec{\zeta}) G_\chi(\vec{x}; \vec{\zeta}) dS(\vec{\zeta}), \quad \chi = \zeta, \eta, \xi \quad (2.24)$$

where  $(n_\zeta, n_\eta, n_\xi)$  are the three components of the unit normal on  $S(\vec{\zeta})$ . The procedure follows as before with  $G(\vec{x}, \vec{\zeta})$  replaced by  $G_\zeta(\vec{x}, \vec{\zeta})$ ,  $G_\eta(\vec{x}, \vec{\zeta})$  and  $G_\xi(\vec{x}, \vec{\zeta})$ ; and  $\sigma$  by  $n_\zeta \gamma$ ,  $n_\eta \gamma$  and  $n_\xi \gamma$ , respectively.

In summary, the evaluation of the pressure  $p$  or normal gradient  $p_n$  at  $N$  collocation points on the BEM boundary  $S$  respectively due to  $N$  source or dipole panels on  $S$  is accomplished in PFFT-BEM using  $O(N)$  memory and  $O(N \log N)$  operations; more precisely  $O(N)$ ,  $O(v^3 N)$ ,  $O(N_g \log N_g)$ ,  $O(N)$ ,  $O(v^3 N)$  respectively in the grid definition, projection, convolution, interpolation and near-field correction PFFT steps, where for shallow water applications,  $N_g$  is typically of the same order as  $N$ .

### 3. Validation/benchmark of PFFT-BEM direct solutions

We first investigate the accuracy and efficiency of the PFFT-BEM method by examining the effects of the numerical element(grid) sizes, the efficiency of different preconditioners and the numerical scalability of the PFFT-BEM method. From this, the optimal PFFT-BEM parameters for shallow water acoustic simulations are obtained. Secondly, using these selected numerical parameters, the capability of PFFT-BEM method in conducting 3D direct numerical simulation for shallow water acoustic problems with large-scale (i.e. large domain size or higher sound frequency) is demonstrated. Two canonical numerical benchmark problems are used here: the Pekeris waveguide and the ASA wedge.

We have conducted other validations which are not shown here. These validations include shallow water environment with an inhomogeneous sound profile (summer sound profile) and bottom Gaussian Canyon, 3D scattering effects by traveling internal waves and 3D sound scattering in the Mouth of the Columbia River (MCR). Good agreements between PFFT-BEM results and available theoretical results/field measurements are obtained for all these cases. The validations are shown in [57].

We begin by considering a Pekeris waveguide problem [3] with flat pressure release boundary on the top and flat penetrable bottom. A unit source with frequency  $f=20\text{Hz}$  is located at depth  $z=36\text{m}$  (from the top surface). The depth of the upper water column is  $H=100\text{m}$ . The bottom layer has an infinite depth. The water column has a density of  $\rho_1=1\text{g/cm}^3$  and a sound speed of  $c_1=1500\text{m/s}$  while the bottom layer has  $\rho_2=1.8\text{g/cm}^3$  and  $c_2=1800\text{m/s}$ . Different computational domain and element(grid) sizes will be used and compared in order to demonstrate the accuracy and efficiency of PFFT-BEM.

### (a) Dependence of accuracy on numerical parameters

Two important factors that determine the accuracy of the PFFT-BEM are investigated: the interpolation from boundary elements to FFT grids and the discretization of FFT-grids and boundary elements.

We first examine the behavior of the interpolation errors. In the far field, the interpolation error is determined by the ratio between the FFT grid size  $h$  and the acoustic wavelength  $\lambda$  (i.e.  $h/\lambda$ ). In the present study, we chose  $h/\lambda$  to equal to  $\Delta l/\lambda$  where  $\Delta l$  is the size of the boundary elements. This ensures that the interpolation error is of the same order as the discretization error in the far field. In the near field, the interpolation error is a function of the polynomial order  $\beta$  of the interpolation function  $H$  where  $\beta=1,2$  denotes linear or quadratic polynomials [35] and  $d/h$  is the critical distance separating the near and far fields.

We compare the  $p_n$  on the top surface (pressure release boundary) and  $p$  on the bottom surface (penetrable boundary) of the Pekeris waveguide obtained using PFFT-BEM with the numerical solutions obtained by conventional BEM. The computational domain size of the Pekeris waveguide is chosen as  $1\text{km} \times 1\text{km} \times 100\text{m}$  with uniform meshing  $\Delta l=h=\lambda/12$ . In Fig.1(a),  $\epsilon$  denotes the average difference between conventional BEM solutions and PFFT-BEM solutions normalized by the conventional BEM solutions (e.g. for  $p$ ,  $\epsilon = \frac{1}{N} \sum_i^N |((p_{BEM})_i - (p_{PFFT})_i)/(p_{BEM})_i|$ ) and is shown as a function of  $d/h$ . It is seen that for both  $\beta=1$  and 2,  $\epsilon$  decays with increasing  $d/h$ , as expected. In addition, the convergence rate of the PFFT-BEM solutions with increasing  $d/h$  are much faster when quadratic interpolation functions ( $\beta=2$ ) are used. To compare computational cost, PFFT-BEM computations with  $\beta=1,2$  are applied to solve the Pekeris waveguide problem using different size of meshing. Using the numerical experiment shown in Fig.1(b), we compare the operation count per iteration  $N_{op}$  for PFFT-BEM using different  $\beta$  and it is seen that  $\beta=2$  uses only slightly more CPU operations per iteration than the  $\beta=1$  scheme. An average relative error of  $\epsilon \sim 1\%$  (i.e. 0.1dB) is used as the standard to judge the methods of interpolation and discretization in the present study. As a result, we have chosen to use the PFFT-BEM parameters as  $\beta=2$ ,  $d/h=3$  for the remainder of the study.

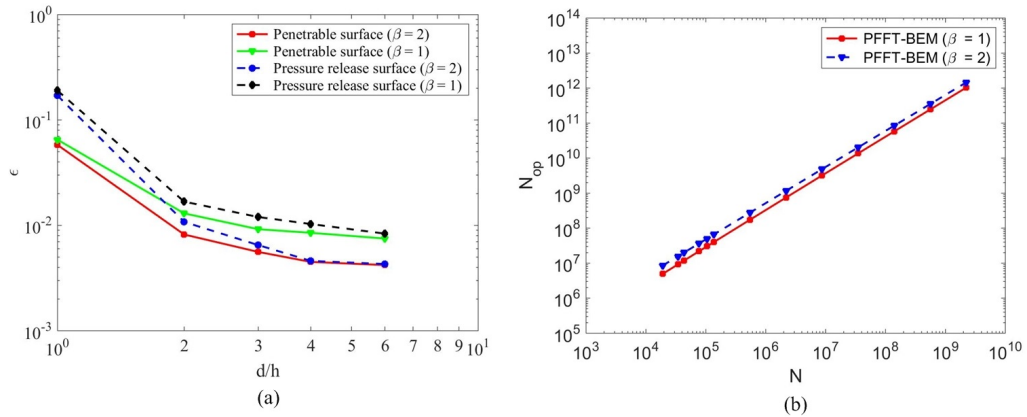


**Figure 1.** (a) Normalized average interpolation errors  $\epsilon$  between the PFFT-BEM and the conventional BEM on different surfaces as a function of  $d/h$ . (b) Comparison of the operation count per iteration step of PFFT-BEM using linear ( $\beta=1$ ) and quadratic ( $\beta=2$ ) interpolation as a function of  $N$ .

To examine the discretization error, we compare our numerical solution of the Pekeris waveguide with the known analytical solution [3] in order to understand the convergence characteristics of the PFFT-BEM numerical predictions. Here, we continue to use that  $d/h=3$

and  $\beta=2$ . The computational domain is  $10\text{km} \times 10\text{km} \times 100\text{m}$ . The boundary element model consists of uniform quadrilateral element with edge length of  $\Delta l$  being equal to  $\lambda/8$  or  $\lambda/12$ . The numerical method computes the transmission loss (TL) along the range at depth of at  $z = 46\text{m}$  and we compare it with the analytical results [3] as shown in Fig.2(a). TL is defined as the ratio in decibels between the acoustics intensity  $I$  at a field point and the intensity  $I_0$  at 1-m distance from the source, i.e.,

$$TL = -10 \log_{10} \frac{I}{I_0} \quad (\text{dB re } 1 \text{ m}) \quad (3.1)$$

The numerical results compare well with the reference result which could validate our numerical method. The numerical results shows a clear convergence to the theoretical solutions when the  $\Delta l$  is decreased from  $\lambda/8$  to  $\lambda/12$ . The total computational time for the Pekeris waveguide case with  $\Delta l = \lambda/8$  is 276.3s with 16 computational nodes.

We then compare the maximum and averaged errors between the analytical results  $p^a$  and the numerical values of pressure  $p^n$  at  $z=46\text{m}$ . These error metrics are defined as

$$\epsilon_{average} = \frac{1}{N} \sum_i^N |((p^n)_i - (p^a)_i)/(p^a)_i|; \quad \epsilon_{max} = \max\{|((p^n)_i - (p^a)_i)/(p^a)_i|; i = 1, \dots, N\}; \quad (3.2)$$

and are shown in Fig.2(b). The errors decrease approximately quadratically with element (and grid) size  $\Delta l/\lambda$  (i.e. decrease linearly with element area) as expected.

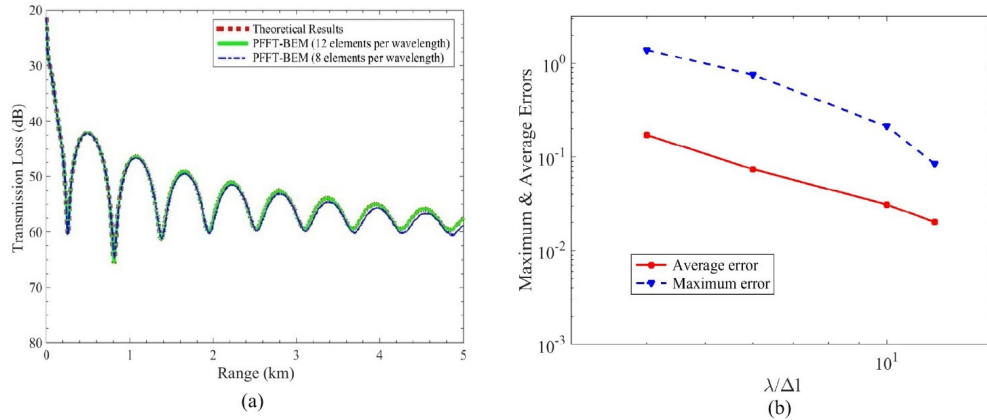


**Figure 2.** (a) Comparison of Transmission Loss (TL) at  $z = 46\text{m}$  as a function of range between the theoretical predictions [3] and the PFFT-BEM. (b) Normalized average  $\epsilon_{average}$  and maximum  $\epsilon_{max}$  errors of  $p$  at  $z=46\text{m}$  obtained using the PFFT-BEM as a function of  $\lambda/\Delta l$ . The slopes  $\kappa$  are approximately equals to -2 for both the maximum and averaged errors.

### (b) Determination of preconditioner

The computational cost in solving Eq.(2.10) is also largely impacted by the convergence rate of the iterative solver. An efficient preconditioner can significantly increase the convergence rate of the iterative solver. In this study, we use a so-called ‘Mesh-based Neighbor (MN)’ preconditioner which has been shown to be useful in different kinds of boundary-value problems (e.g. Harris and Chen [37]). The performance of the MN preconditioner is demonstrated by comparing three cases: the case with Jacobian preconditioner (e.g. Balay *et al.* [38]), the case with MN preconditioner including 2 and 4 neighboring meshes ( $N_m=2$  and 4) and the case without a preconditioner. In

Fig. 3, the MN preconditioner is shown to improve the computational speed of the PFFT-BEM code by nearly two orders of magnitude for the Pekeris waveguide problem.

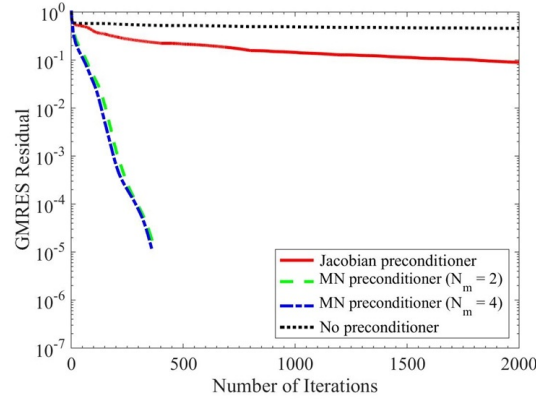


**Figure 3.** GMRES residual as a function of iteration number for the Pekeris waveguide problem with a computational domain of  $25\text{km} \times 15\text{km} \times 100\text{m}$ . The results shown are obtained either without the use of a preconditioner or with either the Jacobian or MN preconditioner.

### (c) PFFT-BEM scalability on processor numbers and unknown numbers

To further increase the numerical capability, the PFFT-BEM is implemented using the PETSc software package which allows for efficient highly scalable algorithms to be developed [38]. To demonstrate the scalability of the parallelized PFFT-BEM, we report the scaling results by comparing the total execution time for a fixed problem as a function of the total processor count. We perform this test using a finely meshed Pekeris waveguide case with a computational domain of size  $10\text{km} \times 10\text{km} \times 100\text{m}$  and element size  $\Delta l = \lambda/16$  which makes  $N = 9.7 \times 10^7$ . We use  $\beta=2$ ,  $d/h=3$  and  $N_m=2$  in this case. The test is carried out using:  $P=[120, 240, 320, 480, 600, 800, 960]$  where  $P$  is the number of processors that are used. As shown in Fig. 4(a), we define a variable called 'speed up' which is defined as the CPU time for a run with  $P$  processor compared with the run with  $P=120$  case. Strong scaling is observed in Fig. 4(a) with the computational speed up being nearly linear with the processor count.

In Fig. 4(b), we plot the operation count  $N_{op}$  of PFFT-BEM per iteration versus different  $N$  for the Pekeris waveguide problem. We use  $\beta=2$ ,  $d/h=3$  and  $N_m=2$  in this case. For comparison, the computational effort of the conventional BEM is also plotted. It can be seen that the computational effort is proportional to  $N$  for PFFT-BEM while that of conventional BEM is proportional to  $N^2$  and much larger than the computational effort of PFFT-BEM. We will further demonstrate the effectiveness of the PFFT-BEM method and its capability in simulating realistic acoustic wave propagation and scattering problems in 3D range dependent environments by examining three canonical shallow water problems: the ASA wedge, a 3D underwater seamount problem, and a 3D rough ocean surface scattering problem. We have chosen to use the PFFT-BEM parameters as  $\beta=2$ ,  $d/h=3$  and  $N_m=2$  in all these benchmark cases. Different grid(element) sizes are used to show the convergence of the numerical results towards the theoretical results. All the computations are performed on parallel HPC platforms with large number of computational nodes that each contains 32 Intel Xeon processors clocked at 2.3GHz and 2GB memory.

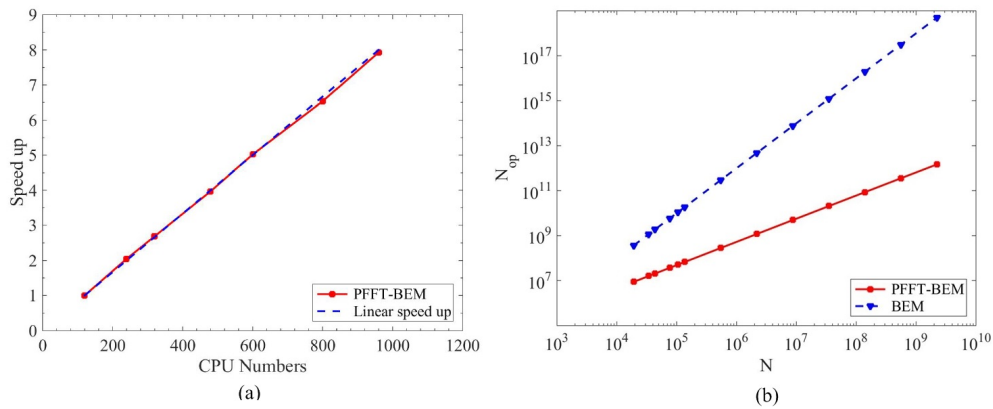


**Figure 4.** (a) CPU scaling for the Pekeris waveguide and fixed  $N = 7 \times 10^6$ , with increasing processors counts, using PFFT-BEM. (b) Comparison of operation count per iteration step of PFFT-BEM method (slope  $\kappa \sim 1$ ) and conventional BEM (slope  $\kappa \sim 2$ ) as a function of  $N$ .

#### (d) Benchmark solutions for the ASA wedge

An idealized wedge problem, shown in Fig.5(a), is used as the second benchmark problem. A 75Hz point source is located at  $(x, y, z) = (0, 0, 100)$  m. The slope of the wedge is  $\pi/36$ . The two-layer computational domain size is  $28\text{km} \times 4\text{km} \times 400\text{m}$ . The water column is homogeneous with sound speed  $c_1 = 1500\text{m/s}$ , density  $\rho_1 = 1\text{g/cm}^3$ , and no medium loss. The bottom is also homogeneous with sound speed  $1700\text{m/s}$  and medium attenuation  $\alpha = 0.5\text{dB}/\lambda$ . The bottom density is equal to  $1.5\text{g/cm}^3$ , which corresponds to a soil bottom. The TL along the  $x$ -axis at  $z = 30\text{m}$  and the TL contour on the horizontal  $x - y$  plane at  $z = 30\text{m}$  obtained from PFFT-BEM are shown in Fig.6(a) and Fig.6(b). In Fig.6(a), the numerical result compares very well with the theoretical result which demonstrates the efficiency and accuracy of the present method for higher frequency cases. The computational resources required for this case is  $N_{node} = 20$  and  $\tau_c \approx 6\text{hrs}$ . In addition, the numerical convergence is also shown by comparing the results with  $\Delta l = \lambda/8$  and  $\Delta l = \lambda/12$  (which makes  $N = 9.7 \times 10^9$ ).

### 4. Model comparisons using PFFT-BEM direct simulations

We compare the predictions obtained by the direct 3D PFFT-BEM computations with existing established models to assess their accuracy and performance in more complex/non-standard environments. Two existing models are examined: one is the axisymmetric coupled mode model for sound scattering by a 3D underwater seamount, and the other is the Kirchhoff approximation and perturbation theory for sound scattering by 3D rough surfaces.

#### (a) Sound Propagation and Scattering Around a 3D Seamount

We conduct a 3D direct numerical study of sound propagation and scattering by an underwater seamount environment. This is a classical three-dimensional problem in which the azimuthal inhomogeneity and 3D effects are important and cannot be neglected. However, fully 3D direct numerical computation requires large computational cost. For example, for a 3D seamount problem with  $f = 400\text{Hz}$  and domain size  $L \sim O(1)\text{km}$ , BEM direct simulation requires  $O(10^{8 \sim 9})$  CPU hours. On the other hand, the efficient PFFT-BEM requires only  $O(10^3)$  CPU hours for the same problem. Theoretical model such as the coupled mode method can provide efficient predictions of 3D sound field around an axisymmetric (conical) seamount [4]. Here, we apply

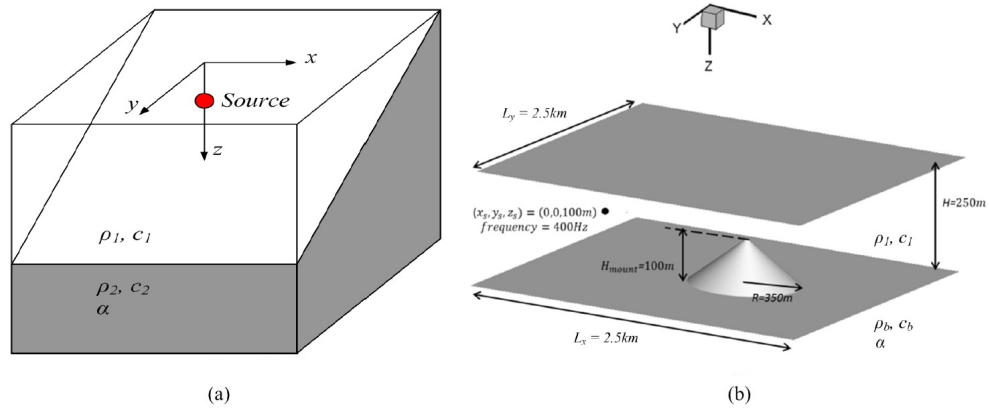


**Figure 5.** (a) Geometry of the underwater ASA wedge, with slope angle  $\pi/36$ . A 75Hz point source is located at  $(x, y, z) = (0, 0, 100)\text{m}$ . The wedge meets the free surface ( $z=0$ ) at  $y=-2000\text{m}$ . (b) Geometry of the underwater seamount. The water depth of the waveguide is 250m. A point source is located at 100m from the water surface and 800m from the center of the seamount. The seamount has a height of 100m and a base with 350m radius.

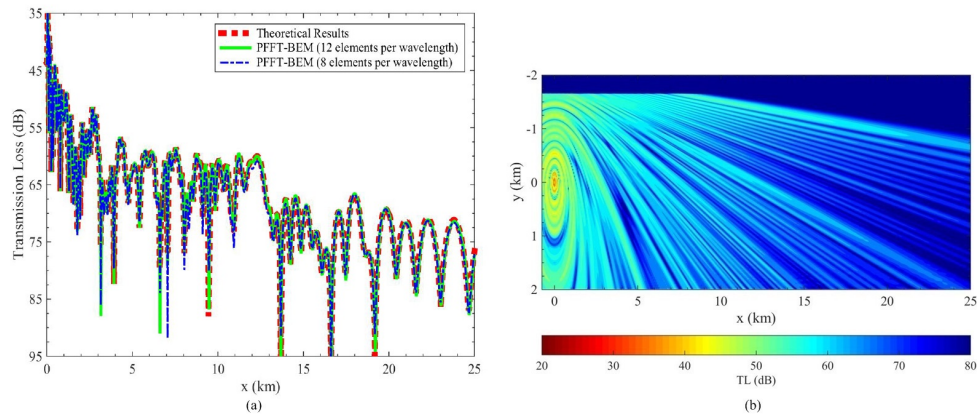


**Figure 6.** (a) TL comparison along the  $x$ -axis at  $z=30\text{m}$  for ASA wedge between the theoretical predictions [33] and the 3D direct simulations by PFFT. (b) TL obtained using PFFT-BEM on the  $x-y$  plane at  $z=30\text{m}$ . Source frequency  $f=75\text{Hz}$  with upper water layer having  $\rho_1=1\text{g/cm}^3$ ,  $c_1=1500\text{m/s}$ , on top of a soil bottom with  $\rho_2=1.5\text{g/cm}^3$ ,  $c_2=1700\text{m/s}$  and a medium attenuation  $\alpha=0.5\text{dB}/\lambda$ .

3D PFFT-BEM direct computation for the 3D shallow water seamount scattering problem with low-mid frequency (up to 400Hz). We investigate the importance of seamount geometry on the acoustics scattering by the seamount. Through these studies, we assess the performance of the axisymmetric coupled mode model. We also investigate the importance of sound frequency on the acoustics scattering by the seamount.

#### (i) Validation against coupled mode method

We consider a seamount waveguide with a pressure-release free surface and a penetrable bottom. The geometry is based on the study by Luo and Schmidt [4], as shown in Fig.5(b). The water column depth  $H=250\text{m}$  with  $c_1=1500\text{m/s}$  and  $\rho_1=1\text{g/cm}^3$ . A point source with unit strength



is placed at  $(x, y, z) = (0, 0, 100)$  m. A conical seamount of height 100 m is located on the bottom at  $(x, y) = (800, 0)$  m. The properties of the seamount is the same as the bottom with  $c_b = 1800$  m/s,  $\rho_b = 2$  g/cm<sup>3</sup> and medium attenuation  $\alpha = 0.1$  dB/ $\lambda$ .

We use a two-layer PFFT-BEM computational domain of size  $2.5\text{ km} \times 2.5\text{ km} \times 250$  m with  $\Delta l = \lambda/8$ . A result using a coupled mode method [4] for this axisymmetric geometry is available for comparison. Fig. 7(a) shows the PFFT-BEM TL results along  $(y, z) = (0, 100)$  m. The grid independence with  $\Delta l$  is established with a separate computation using  $\Delta l = \lambda/12$  and the TL curves are graphically indistinguishable. The PFFT-BEM results compare well with those from [4] with small discrepancies only in the very high loss locations. For comparison, TL along  $(y, z) = (400, 100)$  m is also plotted which show significant difference with transverse distance. The contour plot, Fig. 7(b), shows the complex 3D TL variations in the horizontal plane at the source depth  $z = 100$  m. This fairly low frequency case ( $f = 40$  Hz) is computed with  $N_{\text{node}} = 12$  and  $\tau_c \approx 200$  s.

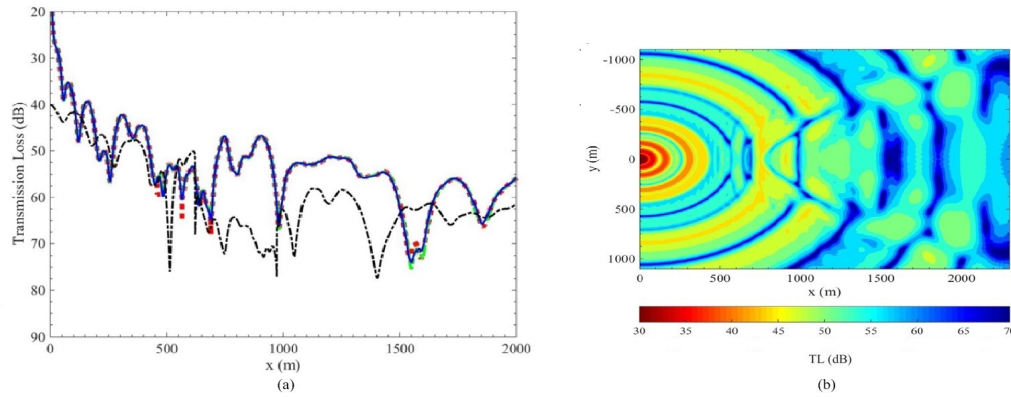


**Figure 7.** (a) TL comparison at different  $x$ —locations with  $(y, z) = (0, 100)$  m for 3D underwater seamount with  $f = 40$  Hz between coupled mode method [4] (red line) and 3D direct simulations by PFFT-BEM with 8 elements per wavelength (blue line) and 12 elements per wavelength (green line); TL at different  $x$ —locations with  $(y, z) = (400, 100)$  m by PFFT-BEM with 12 elements per wavelength (black line); the green and blue line overlap with each other in the figure. (b) TL obtained using PFFT-BEM on the  $x - y$  plane at  $z = 100$  m.

## (ii) Effect of seamount cross section shapes

This numerical method can provide accurate and efficient solutions for 3D underwater bottom features with specified geometries such as a conical seamounts [4]. To assess the applicability of the axisymmetric coupled mode method [4], we study the acoustics scattering by underwater seamounts with different cross section shapes. The geometry of the seamount cross sections is considered to be ellipse. The aspect ratio of the ellipse is defined as  $a = R_y / R_x$ , as shown in Fig. 9, where  $R_y$  ( $R_x$ ) is the radius in the  $y$ —direction ( $x$ —direction). The height of the seamount is fixed at  $H_0 = 100$  m. The source, fluid and bottom properties are the same as those in the conical seamount. For all these cases, PFFT-BEM uses uniform quadrilateral elements with  $\Delta l = \lambda/8$ .

We fix  $R_y = 350$  m and vary  $a$  by changing  $R_x$ . TL in the  $x - y$  plane at  $z = 100$  m is plotted and compared in Fig. 9. From these plots, we see that the TL contour changes significantly even with a small variation in  $a$ . To quantify these differences, in Fig. 8, we further compare the TL in the horizontal plane at depth  $z = 100$  m along the  $x$ —axis for different seamount cross section shapes. We see that relatively small variations in  $a$  can create large changes (up to 10 dB) in TL for both

backscattering and blocking effects. We also fix  $R_x=R$  and vary the aspect ratio by changing  $R_y$ . Similar results are obtained that small variations in  $a$  (due to changes in  $R_y$ ) can induce significant differences in the 3D seamount scattering effects. Details are omitted here and can be found in [57].

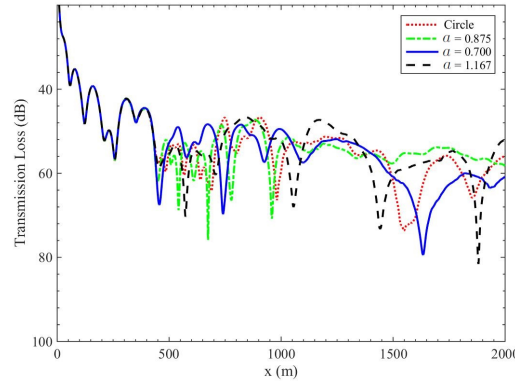


**Figure 8.** TL at different  $x$ -locations with  $(y, z) = (0, 100\text{m})$  for 3D underwater seamount obtained using 3D direct simulations by PFFT-BEM. Here,  $f = 40\text{Hz}$  and the seamount cross sections are circle and ellipses with aspect ratio  $a=0.875, 0.7$  and  $1.167$ .  $R_y$  is fixed at  $350\text{m}$ .

### (iii) Comparison between low- (40 Hz) and mid-frequency (400 Hz) scattering by conical seamount

PFFT-BEM is applicable to general geometries and capable of higher frequencies using HPC. To illustrate the latter, we consider the same conical geometry as in Fig.7 but for  $f=400\text{Hz}$ . Here, we use  $\Delta l = \lambda/12$  which makes  $N = 1.3 \times 10^4$ . Fig.10(a) plots the TL along  $(y, z)=(0, 100)\text{m}$  comparing the  $f=400\text{Hz}$  vs.  $40\text{Hz}$  cases. The backscattering effects from the seamount is clearly more significant for  $f=400\text{Hz}$  with TL nearly  $10\text{dB}$  smaller, for example, in front of the seamount, for the higher-frequency scattering. Fig.10(b) plots the transverse TL variation along  $(x, z)=(800, 100)\text{m}$  (at the apex of the seamount). Comparing the two frequencies, the 3D scattering effects in the azimuthal direction from the seamount is clearly stronger for the  $f=400\text{Hz}$  case. The TL contour in the horizontal plane at the different depths are shown in Fig.11. These highlight the impact of the strong 3D scattering on the TL at different depths. The computational resources required for this  $f=400\text{Hz}$  case are  $N_{\text{node}}=60$  and  $\tau_c \approx 6\text{hrs}$ .

### (b) 3D Sound Scattering by a Rough Surface

Accurate prediction of acoustics scattering from rough surfaces is of importance in modeling the underwater reverberation and forward scattering problems. As an illustration, we consider here the problem of scattering of a plane incident sound wave ( $p_i$ ) by a rough 3D ocean surface on which the pressure release condition is imposed. The angle of the incident wave (scattering wave  $p_s$ ) propagation direction from the mean rough surface is defined as the grazing angle  $\theta_g$  (scattering angle  $\theta_s$ ). This problem can be formulated in terms of the boundary integral equation, as shown in [57]. Direct numerical solution of this problem is however challenging, especially for small  $\theta_g$ , since a large computational domain with the size  $L \gg \lambda / \sin \theta_g$  needs to be employed in order to accurately account for the far-field scattering effects [58], where  $\lambda$  is the acoustic wavelength. To overcome this challenge, several approximate models have



been proposed for the prediction of rough surface scattering statistics. These models include the Kirchhoff approximation and the perturbation theories. Kirchhoff approximation is based on the flat surface assumption that is valid for surfaces with a large radius of curvature. In the Kirchhoff approximation, the shadowing and multi scattering effects are neglected. On the other hand, the perturbation theories are developed in terms of the small parameter  $kh \ll 1$ , where  $h$  is the rms height of the rough surface and  $k$  is the acoustics wavenumber. The details of these approximate models can be found in [57]. By combining these approximate models with the propagation models (such as the parabolic equation (PE) method and ray tracing method), one can predict the reverberation/scattering process by ocean surface and bottom efficiently. It is thus important and necessary to quantify and assess the dependence of the validity of these approximate models on the relevant physical parameters, by comparing with the direct numerical prediction. Most of the existing studies on this are for the 2D problems (e.g. [59]). Shi et al. [60] examined the validity of 3D Kirchhoff approximation for electromagnetic waves with incident waves close to the normal direction of the surface.

We apply direct PFFT-BEM computations to quantify the validity regions of the Kirchhoff approximation and the first- and second-order perturbation theories for 3D acoustics wave scattering from a Gaussian rough surface. We follow [61] and apply the maximum 1-dB error criterion to define the validity region of the approximate theoretical models:

$$|SS_M - SS_N| \leq 1dB \quad (4.1)$$

where the subscripts ( $M$ ) and ( $N$ ) represent the quantities predicted by the approximate model and the numerical PFFT-BEM computation, and  $SS$  denotes the bistatic scattering strength [59]

$$SS = 10 \log_{10}[\sigma(\theta_g, \theta_s)] \quad (4.2)$$

with the scattering cross section  $\sigma(\theta_g, \theta_s)$  defined as

$$\sigma = \frac{\langle |p_s(\theta_g, \theta_s)|^2 \rangle}{E_3} r^2. \quad (4.3)$$

In the above,  $\langle \rangle$  indicates an ensemble average,  $p_s$  represents the scattered wave pressure at the far field range  $r$ , and  $E_3$  is the sound flux through the surface by the incident wave field

$$E_3 = \iint_S p_i(\vec{u}_i \cdot \vec{n}) dS \quad (4.4)$$

where  $\vec{n}$  is the surface normal and  $\vec{u}_i$  is the incident particle velocity on the scattering surface  $S$ . A wide range of grazing angle ( $\theta_g = 2.5^\circ \sim 80^\circ$ ) and random surface roughness ( $0.1 \leq kh \leq 3.0$ ) are considered. The Monte Carlo technique is used to obtain the acoustics scattering statistics with 50 realizations of the Gaussian rough surface. The high efficiency of the PFFT-BEM enables us to perform the requisite direct computations and obtain the assessment of the validity of the approximate models for the 3D problems. In the case of  $\theta_g = 5^\circ$ , for example, the direct BEM simulation requires  $O(10^8)$  CPU hours while the PFFT-BEM simulation requires only  $O(10^3)$  CPU hours.

### (i) 3D effects on the rough surface scattering

Fig.12 shows a sample validity region of the 3D first-order perturbation theory  $\sigma^{(2)}$  in the plane of  $kl$  vs.  $kh$  for  $\theta_g = 45^\circ$ , where  $l$  is the correlation length of the rough surface. (We follow [61] and [59] to use  $\sigma^{(2)}$  and  $\sigma^{(4)}$  for the results by the first- and second-order perturbation theories). To illustrate how the prediction error of the first-order perturbation theory behaves with varying  $kl$  and  $kh$ , in Fig.12, we compare the theoretical solution of  $SS$  over a wide range of scattering angles by the first-order perturbation theory with the benchmark solution of the direct PFFT-BEM computation for four different combinations of  $kl$  and  $kh$ . The comparison indicates that the prediction error of the first-order perturbation theory outside the validity region (defined by (4.1)) generally increases as the distance from the boundary of the validity region becomes larger ((b)  $\rightarrow$  (d) in Fig.12).

In Fig. 13, we compare the validity regions of the 3D first-order perturbation theory ( $\sigma^{(2)}$ ), the 3D second-order perturbation theory ( $\sigma^{(4)}$ ) and the 3D Kirchhoff approximation (KA) for  $\theta_g=45^\circ$ . As expected, the validity region of the second-order perturbation theory becomes larger (i.e. for larger values of  $kl$  and  $kh$ ) comparing to that of the first-order theory. In general, the Kirchhoff approximation is valid at large values of  $kl$  while the first- and second-order perturbation theories are valid at small values of  $kl$ . To see how the 3D surface influences the validity of these approximate models, we also plot the corresponding validity regions in the case of 2D surface from the existing study [59] in Fig. 13. In the 3D case, the validity regions of the first- and second-order perturbation theories and the Kirchhoff approximation are all shifted to the larger  $kl$  regions comparing to the 2D case. Owing to stronger shadowing effects in the 3D case, the validity region of the Kirchhoff approximation decreases from the 2D case. To further assist in understanding the shadowing effect, we compare in Fig. 13 the predictions of SS as a function of  $\theta_s$  by the Kirchhoff approximation with the benchmark solution by the direct PFFT-BEM computations in both 2D and 3D cases with  $kh=1.03$  and  $kl=10.0$ . The error in the prediction of SS by the Kirchhoff approximation is more significant in 3D (Fig. 13(b)) than in 2D (Fig. 13(a)), especially in the backscattering direction. This is consistent with the finding in [58] that the Kirchhoff approximation leads to inaccurate modeling of surface shadowing effects.

## (ii) Grazing angle effects on the rough surface scattering

To illustrate the effect of grazing angle, we compare the backscattering strength (defined as the scattering strength at  $\theta_s = \pi - \theta_g$ ) calculated using the second-order perturbation theory, the Kirchhoff approximation and the direct PFFT-BEM computation. Fig. 14 shows the comparison with grazing angle down to  $2.5^\circ$ . (At  $\theta_g=2.5^\circ$ , the computation uses  $N=4.1 \times 10^7$  with  $\Delta l=\lambda/8$ ). We also plot the result from Lambert's law in Fig. 14 for comparison. Lambert's law is often used to estimate the bottom scattering strength from very rough ocean bottoms. A good review of Lambert's law can be found in [3]. As shown in Fig. 14, the second-order perturbation theory provides a reasonably accurate prediction for incident grazing angle  $\theta_g \gtrsim 20^\circ$  while the Kirchhoff approximation remains valid for  $\theta_g \gtrsim 60^\circ$ . Lambert's law generally gives a good prediction at small grazing angles. For rougher ocean surfaces, an accurate prediction by Lambert's law can be obtained for  $\theta_g$  up to  $30^\circ$ , as shown in Fig. 14(b). The comparisons in Fig. 14 indicate that for 3D rough surfaces with large  $kl$  and moderate  $kh$ , direct numerical simulation is required to obtain an accurate backscattering prediction, especially for low grazing angles.

## 5. Conclusion

We develop an efficient multi-layer boundary element method (BEM) for direct 3D simulations of large-scale shallow water acoustic problems. The medium inhomogeneity is accounted for by a coupled multi-layer BEM model. A main development is the use of Pre-corrected Fast Fourier Transform (PFFT) approach to reduce the computational cost from  $O(N^{2\sim 3})$  to  $O(N \log N)$  where  $N$  is the number of unknowns on the BEM computational domain boundary. PFFT-BEM is particularly suitable for parallelization, and the method is implemented on massively parallel high-performance computing (HPC) platforms achieving near-linear scaling with number of processors. PFFT-BEM allows us to perform routine multi-layer 3D direct simulations of low-mid frequency acoustics over kilometer ranges.

PFFT-BEM has been validated extensively against existing theoretical and computational results with excellent comparisons. We document here, as examples, comparisons to theoretical solutions for the Pekeris waveguide and the Acoustical Society of America (ASA) wedge. The computational efficacy of direct large-scale 3D PFFT-BEM solutions allows us to evaluate the accuracy and range of validity of established approximate/specialized models. We present here assessment of two canonical models: axisymmetric coupled mode model for 3D seamount; and Kirchhoff approximation and perturbation theory for 3D rough surface scattering. For the 3D seamount problem, we characterize and quantify the effects of seamount geometry and sound

source frequencies on the 3D sound scattering field. We find that the acoustics scattering has a strong dependence on seamount height and cross section shape, and source frequency. For 3D rough ocean surface scattering, we quantify the ranges of validity of the approximation models in terms of 3D scattering effects, surface roughness and correlation length, and incidence angle of the sound source. We show how the Kirchhoff approximation and the perturbation theory become insufficiently accurate for 3D rough surface scattering with low grazing angles.

**ACKNOWLEDGMENT:** This work was supported by the Office of Naval Research (N00014-16-1-2200) and was granted access to the HPC resources provided by the DOD HPC Modernization Program. Lawrence Livermore National Laboratory is operated by Lawrence Livermore National Security, LLC, for the U.S. Department of Energy, National Nuclear Security Administration under Contract DE-AC52-07NA27344. This work was supported in part by funding from the Lawrence Fellowship program (LLNL-JRNL-751232).

## References

1. H. P. Buckner, "A simple 3-D gaussian beam sound propagation model for shallow water," *J. Acoust. Soc. Am.* **95**(5), 2437–2440 (1994).
2. M. Porter, "The Bellhop manual and user guide: Preliminary draft," (2011), Heat, Light, and Sound Research, Inc., Tech. Rep.
3. F. Jensen, W. Kuperman, M. Porter, and H. Schmidt, *Computational Ocean Acoustics* (Springer Science and Business Media, 2011).
4. W. Luo and H. Schmidt, "Three-dimensional propagation and scattering around a conical seamount," *J. Acoust. Soc. Am.* **125**(1), 52–56 (2009).
5. H. Schmidt, "Safari: Seismo-Acoustic Fast Field Algorithm for Range-Independent environments. User's Guide ( No. SACLANTCEN-SR-113)," (1988), SACLANT Undersea Research Centre, La Spezia, Italy.
6. A. A. Shmelev, J. F. Lynch, Y. T. Lin, and H. Schmidt, "Three-dimensional coupled mode analysis of internal-wave acoustic ducts," *J. Acoust. Soc. Am.* **135**(5), 2497–2512 (2014).
7. M. Badiéy, B. G. Katsnelson, J. F. Lynch, S. Pereselkov, and W. L. Siegmann, "Measurement and modeling of three-dimensional sound intensity variations due to shallow-water internal waves," *J. Acoust. Soc. Am.* **117**(2), 613–625 (2005).
8. M. S. Ballard, "Modeling three-dimensional propagation in a continental shelf environment," *J. Acoust. Soc. Am.* **131**(3), 1969–1977 (2012).
9. J. F. Lynch, Y. T. Lin, T. F. Duda, and A. E. Newhall, "Acoustic ducting, reflection, refraction, and dispersion by curved nonlinear internal waves in shallow water," *IEEE J. Ocean. Eng.* **35**(1), 12–27 (2010).
10. F. D. Tappert, *The parabolic approximation method*, 224–287, Lecture Notes in Physics (Springer, Berlin, Heidelberg).
11. Y. T. Lin, J. M. Collis, and T. F. Duda, "A three-dimensional parabolic equation model of sound propagation using higher-order operator splitting and Padé approximants," *J. Acoust. Soc. Am.* **132**(5), EL364–EL370 (2012).
12. Y. T. Lin, T. F. Duda, and A. E. Newhall, "Three-dimensional sound propagation models using the parabolic-equation approximation and the split-step Fourier method," *J. Comput. Acoust.* **21**(1), 1250018 (2013).
13. F. Sturm, "Numerical study of broadband sound pulse propagation in three-dimensional oceanic waveguides," *J. Acoust. Soc. Am.* **117**(3), 1058–1079 (2005).
14. M. D. Collins and R. B. Evans, "A two-way parabolic equation for acoustic backscattering in the ocean," *J. Acoust. Soc. Am.* **91**(3), 1357–1368 (1992).
15. J. F. Lingeitch, M. D. Collins, M. J. Mills, and R. B. Evan, "A two-way parabolic equation that accounts for multiple scattering," *J. Acoust. Soc. Am.* **112**(2), 476–480 (2002).
16. D. Zhu and L. B. Bjørnø, "A three dimensional, two-way, parabolic equation model for acoustic backscattering in a cylindrical coordinate system," *J. Acoust. Soc. Am.* **108**(3), 889–898 (2000).
17. M. S. Ballard, B. M. Goldsberry, and M. J. Isakson, "Normal mode analysis of three-dimensional propagation over a small-slope cosine shaped hill," *J. Comput. Acoust.* **23**(3), 1550005 (2015).

18. C. X. Xu, J. Tang, S. C. Piao, J. Q. Liu, and S. Z. Zhang, "Developments of parabolic equation method in the period of 2000–2016," *Chinese Physics B* **25**(12), 124315 (2016).
19. A. Bottero, P. Cristini, D. Komatitsch, and M. Asch, "An axisymmetric time-domain spectral-element method for full-wave simulations: Application to ocean acoustics," *J. Acoust. Soc. Am.* **140**(5), 3520–3530 (2016).
20. J. A. F. Santiago and L. C. Wrobel, "A boundary element model for underwater acoustics in shallow water," *Comput. Model. Eng. Sci.* **1**(3), 73–80 (2000).
21. C. P. Vendhan, G. C. Diwan, and S. K. Bhattacharyya, "Finite-element modeling of depth and range dependent acoustic propagation in oceanic waveguides," *J. Acoust. Soc. Am.* **127**(6), 3319–3326 (2010).
22. M. Isakson, B. Goldsberry, and N. Chotiros, "A three-dimensional, longitudinally-invariant finite element model for acoustic propagation in shallow water waveguides," *J. Acoust. Soc. Am.* **136**(3), EL206–EL211 (2014).
23. Z. Xie, R. Matzen, P. Cristini, D. Komatitsch, and R. Martin, "A perfectly matched layer for fluid-solid problems: Application to ocean-acoustics simulations with solid ocean bottoms," *J. Acoust. Soc. Am.* **140**(1), 165–175 (2016).
24. P. Cristini and D. Komatitsch, "Some illustrative examples of the use of a spectral-element method in ocean acoustics," *J. Acoust. Soc. Am.* **131**(3), EL229–EL235 (2012).
25. A. J. Burton and G. F. Miller, "The application of integral equation methods to the numerical solution of some exterior boundary-value problems," *Proc. Royal Soc. London A* **323**, 201–210 (1971).
26. L. Godinho, A. Tadeu, and F. J. F. G. Branco, "3D acoustic scattering from an irregular fluid waveguide via the BEM," *Eng. Anal. Boundary Element* **25**(3), 443–453 (2001).
27. A. Pereira, A. Tadeu, L. Godinho, and J. A. F. Santiago, "2.5D BEM modeling of underwater sound scattering in the presence of a slippage interface separating two flat layered regions," *Wave Motion* **48**(8), 676–692 (2010).
28. S. Keuchel, K. Vater, and O. V. Estorff, "hp fast multipole boundary element method for 3D acoustics," *Int. J. for Numer. Meth. in Eng.* **110**(9), 842–861 (2017).
29. Z. Yan and X. Gao, "The development of the pfft accelerated bem for 3-D acoustic scattering problems based on the burton and miller's integral formulation," *Eng. Anal. Boundary Element* **37**(2), 409–418 (2013).
30. M. Xue, H. Xu, Y. Liu, and D. K. Yue, "Computations of fully nonlinear three-dimensional wave-wave and wave-body interactions. part 1. dynamics of steep three-dimensional waves," *J. Fluid Mech.* **438**, 11–39 (2001).
31. J. R. Phillips and J. K. White, "A precorrected-FFT method for electrostatic analysis of complicated 3-D structures," *IEEE Trans. Comput. Aided Des. Integr. Circuits Syst.* **16**(10), 1059–1072 (1997).
32. H. Yan and Y. Liu, "An efficient high-order boundary element method for nonlinear wave-wave and wave-body interactions," *J. Comput. Phys.* **230**(2), 402–424 (2011).
33. G. B. Deane and M. J. Buckingham, "An analysis of the three-dimensional sound field in a penetrable wedge with a stratified fluid or elastic basement," *J. Acoust. Soc. Am.* **93**(3), 1319–1328 (1993).
34. T. W. Wu, "On computational aspects of the boundary element method for acoustic radiation and scattering in a perfect waveguide," *J. Acoust. Soc. Am.* **96**(6), 3733–3743 (1994).
35. See Supplementary materials at [URL will be inserted by AIP] for the method to construct matrix H.
36. S. Robinson, P. Lepper, and R. Haxelwood, "Good practice guide for underwater noise measurement," (2014), NPL Good Practice Guide.
37. P. J. Harris and K. Chen, "On efficient preconditioners for iterative solution of a Galerkin boundary element equation for the three-dimensional exterior Helmholtz problem," *J. of Comput. and appl. Math.* **156**(2), 303–318 (2003).
38. S. Balay, S. Abhyankar, M. Adams, J. Brown, P. Brune, K. Buschelman, L. D. Dalcin, V. Eijkhout, W. Gropp, D. Kaushik, and W. S. Knepley, "Petsc users manual revision 3.8.," (2017), Argonne National Lab, Argonne, IL, United States.
39. Ji, H., Xu, X., Guo, X., Ye, S., Chen, J., and Yang, X. (2016). "Direct fvm simulation for sound propagation in an ideal wedge Shock and vibration **1**," 1–9.
40. Caley, M. S., and Duncan, A. (2016). "Wide-band shallow acoustic channel simulation with realistic doppler and delay spreading for 3d evolving rough surfaces Underwater Communications and Networking Conference (UComms) *IEEE Third*," 1.

41. Reilly, S. M., Potty, G. R., and Goodrich, M. (2016). "Computing acoustic transmission loss using 3d gaussian ray bundles in geodetic coordinates *Journal of Computational Acoustics* **24.01**," 1650007.
42. Collins, M. D. (2012). "A single-scattering correction for the seismo-acoustic parabolic equation *J. Acoust. Soc. Am.* **131.4**," 2638–2642.
43. Rodriguez, O. C., Sturm, F., Petrov, P., and Porter, M. (2017). "Three-dimensional model benchmarking for cross-slope wedge propagation *Proceedings of Meetings on Acoustics* **30.1**," 173.
44. Lin, Y., Duda, T. F., Emerson, C., Gawarkiewicz, G., Newhall, A. E., Calder, B., Lynch, J. F., Abbot, P., Yang, Y. J., and Jan, S. (2015). "Experimental and numerical studies of sound propagation over a submarine canyon northeast of taiwan *IEEE Journal of Oceanic Engineering* **40.1**," 237–249.
45. Heaney, K. D., and Campbell, R. L. (2017). "Three dimensional parabolic equation modeling of mesoscale eddy deflection *J. Acoust. Soc. Am.* **139.2**," 918–926.
46. Megan, B. S. (2012). "Modeling three dimensional propagation in a continental shelf environment *J. Acoust. Soc. Am.* **131.3**," 1969–1977.
47. Megan, B. S. (2015). "Coupled mode analysis of three dimensional propagation over a cosine shaped hill *J. Acoust. Soc. Am.* **137.4**," 2419.
48. Kuperman, W. A., and Lynch, J. F. (2004). "Shallow-water acoustics *Physics Today* **57.10**," 55–61.
49. Lin, Y. T., and Duda, T. F. (2012). "A higher-order split-step Fourier parabolic-equation sound propagation solution scheme *J. Acoust. Soc. Am.* **132.2**," EL61–EL67.
50. Feit, M. D., and Fleck, J. A. (1978). "Light propagation in graded-index optical fibers *Appl. Optics* **17.24**," 3990–3998.
51. Sturm, F. (2016). "Leading-order cross term correction of three-dimensional parabolic equation models *J. Acoust. Soc. Am.* **139.1**," 263–270.
52. Collins, M. D., and Westwood, E. K. (1991). "A higher-order energy-conserving parabolic equation for range dependent ocean depth, sound speed, and density *J. Acoust. Soc. Am.* **89.3**," 1068–1075.
53. Yan, Z. Y., Zhang, J., and Ye, W. (2010a). "Rapid solution of 3-d oscillatory elastodynamics using the pfft accelerated bem *Eng. Anal. Boundary Element* **34.11**," 956–962.
54. Masters, N., and Ye, W. (2004). "Fast bem solution for coupled 3d electrostatic and linear elastic problems *Eng. Anal. Boundary Element* **28.9**," 1175–1186.
55. Xiao, J., Ye, W., Cai, Y., and Zhang, J. (2012). "Precorrected fft accelerated bem for large scale transient elastodynamic analysis using frequency domain approach *Int. J. Numer. Meth Eng.* **90.1**," 116–134.
56. Yan, Z. Y., Zhanga and W. Ye, J., and Yu, T. X. (2010a). "Numerical characterization of porous solids and performance evaluation of theoretical models via the precorrected-fft accelerated bem *Computer Modeling in Engineering and Sciences (CMES)* **55.1**," 33.
57. C. Li, "An efficient multi-layer boundary element method for direct computation of sound propagation in shallow water environments," Ph.D. thesis, Massachusetts Institute of Technology, Cambridge, Massachusetts, 2019.
58. E. I. Thorsos, "The validity of the kirchhoff approximation for rough surface scattering using a gaussian roughness spectrum," *J. Acoust. Soc. Am.* **83.1**, 78–92 (1988).
59. P. J. Kaczkowski, J. Peter, and E. I. Thorsos, "Application of the operator expansion method to scattering from one dimensional moderately rough dirichlet random surfaces," *J. Acoust. Soc. Am.* **96.2**, 957–972 (1994).
60. F. Shi, W. Choi, M. J. S. Lowe, E. A. Skelton, and R. V. Craster, "The validity of kirchhoff theory for scattering of elastic waves from rough surfaces," *Proceedings of the Royal Society of London A: Mathematical, Physical and Engineering Sciences* **471**, 2178 (2015).
61. E. I. Thorsos and J. R. Darrell, "The validity of the perturbation approximation for rough surface scattering using a gaussian roughness spectrum," *J. Acoust. Soc. Am.* **86.1**, 261–277 (1989).



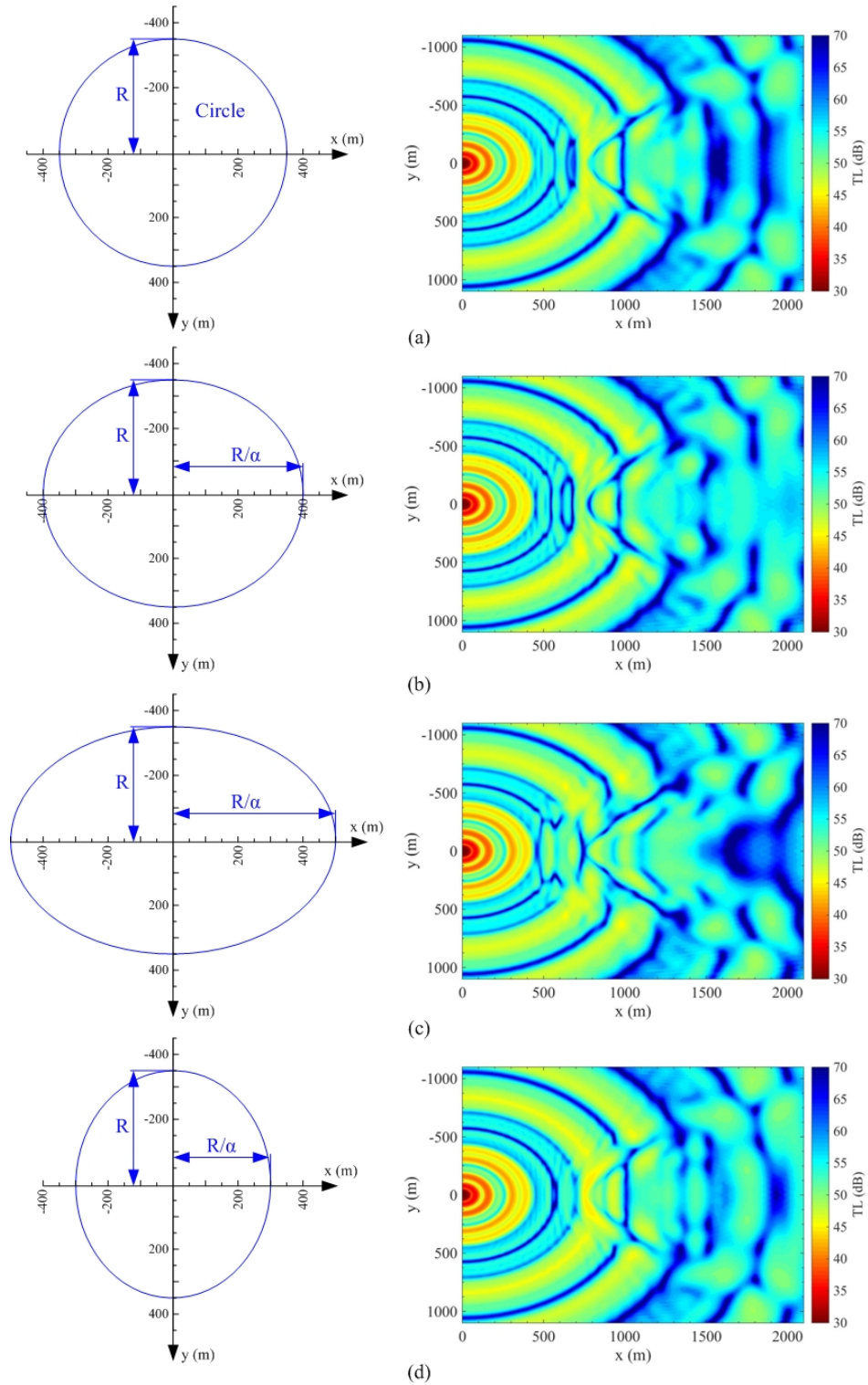


**Figure 9.** Seamount cross section shape at bottom (left) and TL at xy plane ( $z=100\text{m}$ ) obtained using 3D direct simulations by PFFT-BEM (right). Here,  $f = 40\text{Hz}$  and seamount cross sections are (a) circle, (b) ellipse with  $a=0.875$ , (c) ellipse with  $a=0.7$  and (d) ellipse with  $a=1.167$ .  $R_y$  is fixed at  $350\text{m}$ .

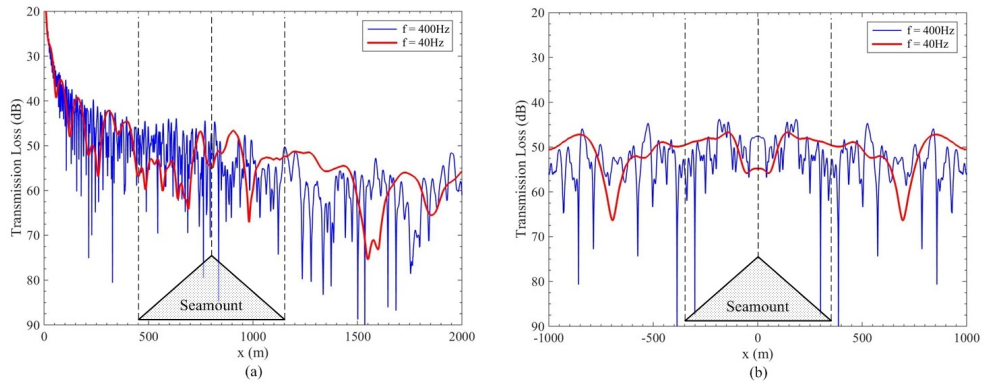


**Figure 10.** (a) TL at different  $x$ -locations with  $(y, z) = (0, 100)$  m and (b) TL at different  $y$ -locations with  $(x, z) = (800, 100)$  m for the 3D underwater conical seamount obtained by PFFT-BEM for  $f = 400$  Hz and 40 Hz.

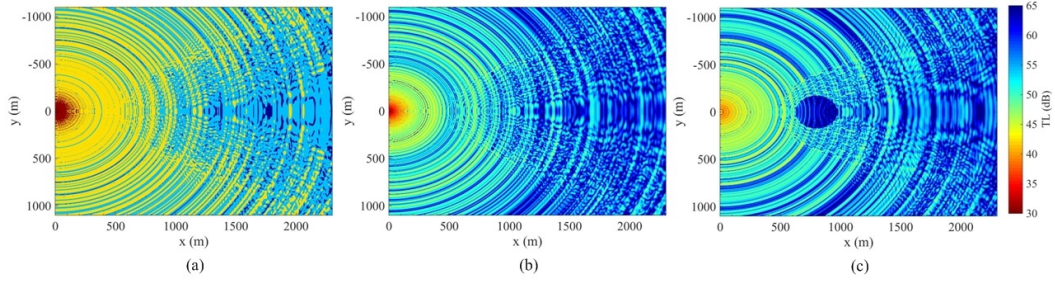


**Figure 11.** Contour of TL on the  $x - y$  plane at (a)  $z = 100$  m, (b)  $z = 200$  m and (c)  $z = 245$  m for the 3D underwater conical seamount obtained using PFFT-BEM. ( $f = 400$  Hz)

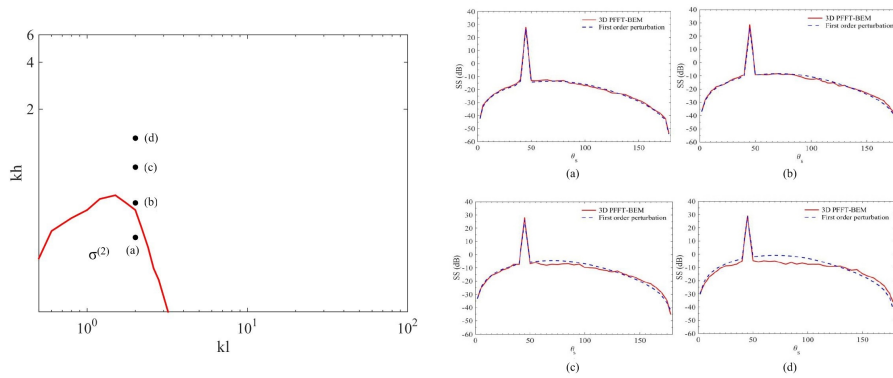


**Figure 12.** Left column: 3D validity region of  $\sigma^{(2)}$  (i.e. under the solid line) of the first-order perturbation theory for  $\theta_g = 45^\circ$ , obtained by comparison with the direct PFFT-BEM computation. Right column: Comparison of the SS obtained by the direct PFFT-BEM computation (solid line) and the first-order perturbation theory (dashed line) with  $(kl, kh) = (2.0, 0.3)$  (a),  $(2.0, 0.55)$  (b),  $(2.0, 0.85)$  (c), and  $(2.0, 1.3)$  (d). The locations of (a), (b), (c) and (d) in the validity region are also marked. In PFFT-BEM computations, the domain size  $L = 50\lambda$ .

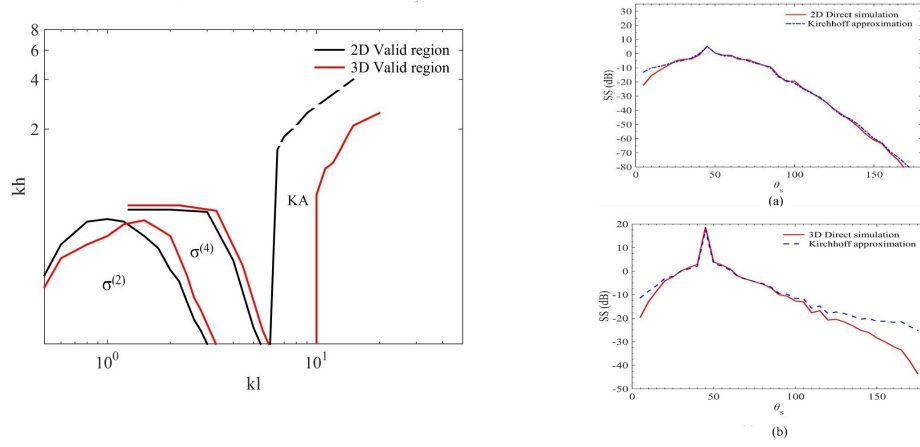


**Figure 13.** Left column: Comparisons of 3D validity regions (red lines) of the first-order ( $\sigma^{(2)}$ ) and second-order ( $\sigma^{(4)}$ ) perturbation theories and Kirchhoff approximation (KA) with the corresponding 2D validity regions (black lines) from [59] for  $\theta_g = 45^\circ$ . Right column: Comparison of SS obtained by the Kirchhoff approximation (dashed line) and direct PFFT-BEM computation (solid line) for 2D (a) and 3D (b) surfaces with  $kh = 1.03$  and  $kl = 10.0$ .

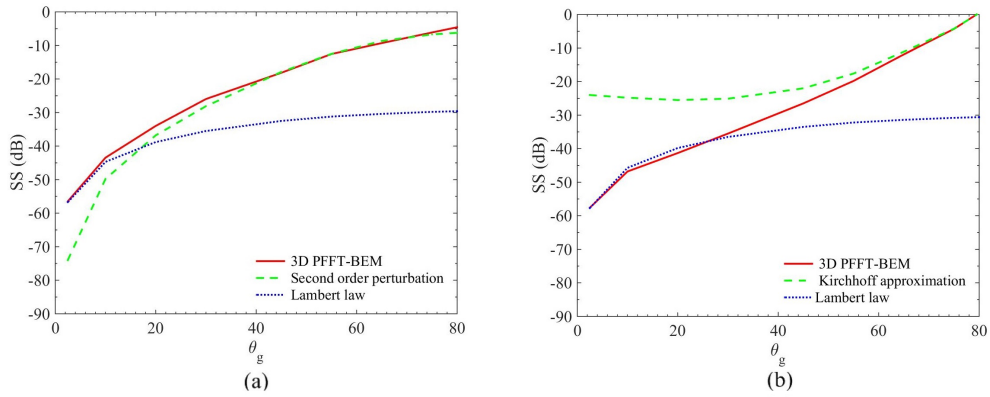


**Figure 14.** (a) Comparisons of SS in the backscattering direction as a function of grazing angle  $\theta_g$  obtained by the second-order perturbation theory (dashed line), Lambert law (dotted line) and direct PFFT-BEM computation (solid line) for  $kl=2.6$  and  $kh=0.65$ . (b) Comparisons of SS in the backscattering direction as a function of grazing angle  $\theta_g$  obtained by the Kirchhoff approximation (dashed line), Lambert law (dotted line) and direct PFFT-BEM computation (solid line) for  $kl=15$  and  $kh=1.33$ .